PNAS RESEARCH ARTICLE | APPLIED BIOLOGICAL SCIENCES ENGINEERING

Magnetic soft microrobots for erectile dysfunction therapy

Shuting Wang[a,b,c,1], Zhenqing Wang[d,1], Zongshan Shen[e,1], Min Zhang[f,1], Dongdong Jin[g], Ke Zheng[h], Xuemin Liu[a], Muyuan Chai[a], Zhenxing Wang[a], Ani Chi[a], Serge Ostrovidov[i], Hongkai Wu[j], Dan Shao[a,k,l], Guihua Liu[m], Kai Wu[a,2], Kam W. Leong[a,2], and Xuetao Shi[a,b,c,2]

Affiliations are included on p. 11.

Edited by David Weitz, Harvard University, Cambridge, MA; received April 24, 2024; accepted October 8, 2024

Erectile dysfunction (ED) is a major threat to male fertility and quality of life, and mesenchymal stromal cells (MSCs) are a promising therapeutic option. However, therapeutic outcomes are compromised by low MSC retention and survival rates in corpus cavernosum tissue. Here, we developed an innovative magnetic soft microrobot comprising an ultrasoft hydrogel microsphere embedded with a magnetic nanoparticle chain for MSC delivery. This design also features phenylboronic acid groups for scavenging reactive oxygen species (ROS). With a Young's modulus of less than 1 kPa, the ultrasoft microrobot adapts its shape within narrow blood vessels, ensuring a uniform distribution of MSCs within the corpus cavernosum. Our findings showed that compared with traditional MSC injections, the MSC delivery microrobot (MSC-Rob) significantly enhanced MSC retention and survival. In both rat and beagle ED models, MSC-Rob treatment accelerated the repair of corpus cavernosum tissue and restored erectile function. Single-cell RNA sequencing (scRNA-seq) revealed that MSC-Rob treatment facilitates nerve and blood vessel regeneration in the corpus cavernosum by increasing the presence of regenerative macrophages. Overall, our MSC-Rob not only advances the clinical application of MSCs for ED therapy but also broadens the scope of microrobots for other cell therapies.

soft microrobots | mesenchymal stromal cells | erectile dysfunction | immunomodulation

Erectile dysfunction (ED) is the most common male sexual dysfunction and is often accompanied by pathophysiological processes such as vascular endothelial dysfunction and immune homeostasis disorders (1). It affects 50% of men aged 40 to 70 y and reflects overall individual health (2). Although traditional drug therapy is temporarily effective, long-term drug administration with potential side effects is unavoidable (3). Mesenchymal stromal cells (MSCs) have been demonstrated to be effective in treating various diseases, such as spinal cord injury (4), cardiovascular diseases (5), and COVID-19(6), through paracrine effects and multilineage differentiation to promote angiogenesis and antifibrosis and restore immune homeostasis (7–9). However, the high blood flow velocity and increased reactive oxygen species (ROS) level in the corpus cavernosum microenvironment of ED patients result in extremely poor retention and survival of MSCs after transplantation, compromising their therapeutic effects (10, 11). Therefore, a reasonable strategy to improve the retention and survival of MSCs in corpus cavernosum tissue is urgently needed.

Microrobots have been extensively investigated for their ability to deliver therapeutic agents (such as drugs, cells, and exosomes), demonstrating effective navigation to target areas and improved retention of these agents (12–16). In particular, magnetically driven microrobots, owing to their deep penetration and safety, have emerged as the optimal choice for navigating and propelling within small-scale structures within the human body (17–19). Researchers have developed various porous magnetic microrobots for MSC delivery (20), creating platforms for medical applications such as knee cartilage regeneration (21), stomach ulcer healing (18), and neuronal differentiation (22). However, the application of microrobots for corpus cavernosum tissue repair has not been sufficiently explored. The intricate microenvironment of corpus cavernosum tissue poses significant physical challenges for the delivery of cells using microrobots, including the intricacy of the cavernous sinuses, numerous narrow blood vessels, and the densely crowded heterogeneous fluid environment; these challenges impede the progression of microrobots toward their intended targets and may lead to blockage of blood vessels. Therefore, the development of shape-adaptive magnetic microrobots, allowing for their inherent structural adaptability to undergo significant deformation in complex vascular environments and thus avoiding blockage of entry into the target, represents an inspiring therapeutic strategy for treating ED.

Significance

Erectile dysfunction (ED), a prevalent form of sexual dysfunction, significantly affects fertility and quality of life. Mesenchymal stromal cell (MSC) therapies show promise for ED treatment, yet challenges such as low tissue retention and poor MSC survival in corpus cavernosum tissue limit their efficacy. In this study, we introduce a shape-adaptive and reactive oxygen species (ROS)-scavenging microrobot designed to overcome the challenges of vascularization and optimize MSC delivery. The microrobot enhances MSC retention and survival in corpus cavernosum tissue. In both rat and beagle models of ED, treatment with MSC-laden microrobots (MSC-Rob) promoted restored erectile function. Our results indicate that ED could be reversed via this approach, providing a promising outlook for its feasibility in human applications.

Author contributions: S.W., K.W.L., and X.S. designed research; S.W., Z.W., D.J., Z.W., and A.C. performed research; S.W. and K.W. contributed new reagents/analytic tools; S.W., Z.S., M.Z., M.C., D.S., and G.L. analyzed data; and S.W., Z.W., Z.S., D.J., K.Z., X.L., S.O., H.W., K.W., K.W.L., and X.S. wrote the paper.

The authors declare no competing interest.

This article is a PNAS Direct Submission.

[1]S.W., Z.W., Z.S., and M.Z. contributed equally to this work.

[2]To whom correspondence may be addressed. Email: kaiwu@scut.edu.cn, kam.leong@columbia.edu, or shxt@scut.edu.cn.

This article contains supporting information online at https://www.pnas.org/lookup/suppl/doi:10.1073/pnas.2407809121/-/DCSupplemental.

Published November 18, 2024.

Here, we developed an ultrasoft MSC delivery microrobot (MSC-Rob) system for the treatment of ED by embedding magnetically aligned nanoparticles (NPs) into polyethylene glycol (PEG)-based hydrogel microspheres (Fig. 1*A*). This design aims to prevent blockages and improve the retention of MSCs in the corpus cavernosum. Additionally, phenylboronic acid groups were grafted onto microrobots to scavenge ROS, thereby enhancing the survival rates of MSCs (Fig. 1*B*). We evaluated the controllability of the microrobots by analyzing their movement in various biological media, assessing their shape adaptability, and observing their upstream motion. Furthermore, the retention capacity of MSC-Rob in corpus cavernosum tissue was examined through both in vitro and in vivo experiments. The therapeutic efficacy of MSC-Rob was evaluated using rat and beagle models of ED, and the therapeutic mechanism was explored through single-cell RNA sequencing (scRNA-seq). Our MSC-Rob system thus represents a unique and effective approach to augment the therapeutic impacts of MSCs on patients with ED.

Results

Microrobot Construction. The soft microrobots were prepared using a straightforward emulsification method. Encapsulating Fe_3O_4 nanoparticles (NPs) approximately 10 nm in diameter

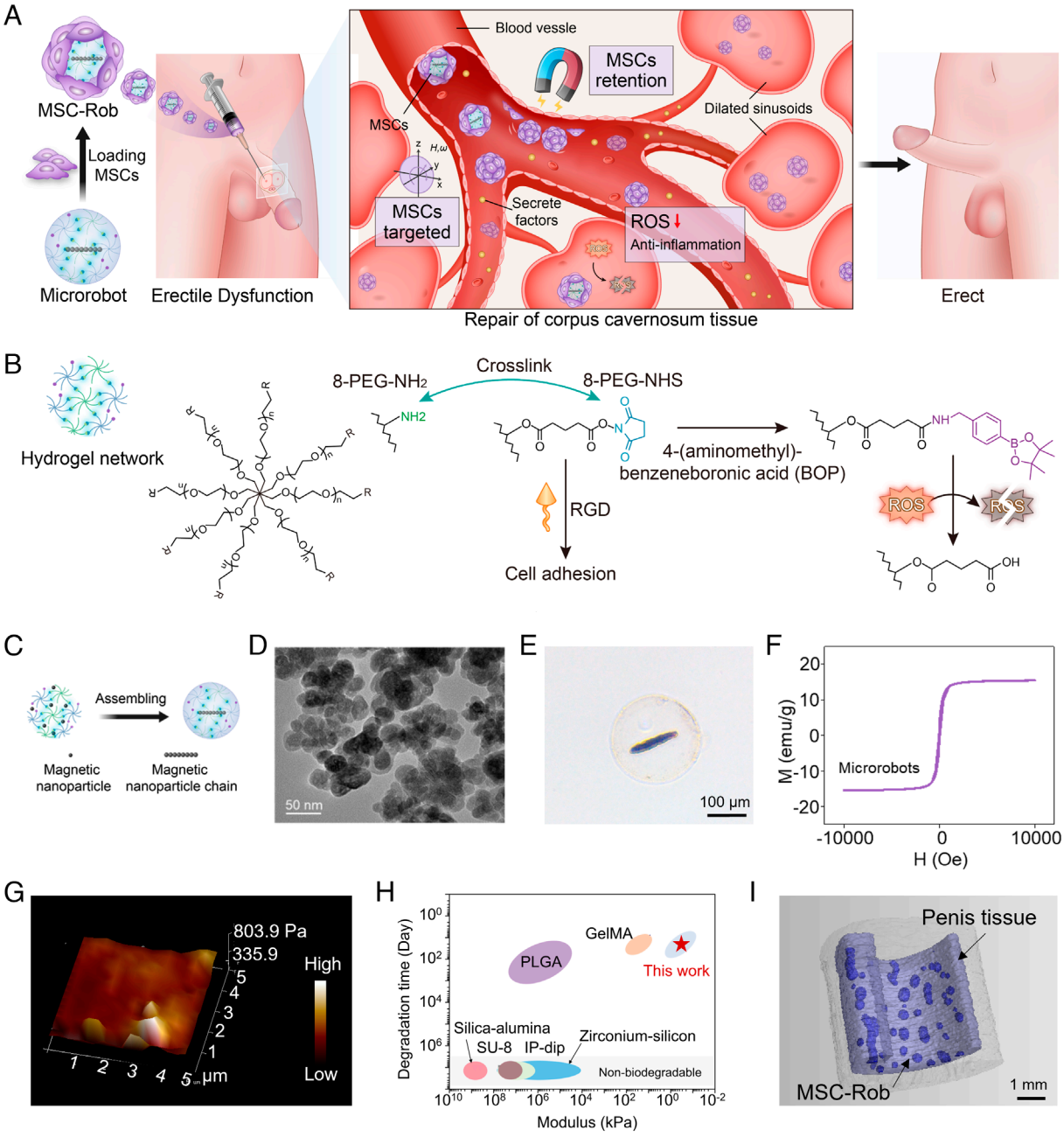

Fig. 1. Construction and characteristics of microrobots. (*A*) Schematic depicting the use of MSC-Rob for the treatment of ED. Drawing inspiration from magnetotactic bacteria, magnetic nanoparticles were arranged in chains within microgels to create microrobots onto which MSCs were loaded. (*B*) Diagram of microrobot components. (*C*) Diagram of magnetic NPs assembled into the chain-like structures in the hydrogel network. (*D*) TEM images showing the surface morphology of the magnetic NP. (*E*) High-resolution XPS graphs showing the composition of the microrobots. (*F*) Magnetic hysteresis curves showing the paramagnetic properties of the microrobots, where M and H represent the magnetization and magnetic flux, respectively. (*G*) 3D Young's modulus maps showing the mechanical properties of 5 μm microrobots at a 1.5% solid content. (*H*) A comparative analysis of the modulus and degradation time of cell-loaded microrobots reported in the literature. (*I*) μCT images of the MSC-Rob in an ex vivo porcine penis tissue.

(Fig. 1 *C* and *D* and *SI Appendix*, Fig. S1), which are crucial for magnetic propulsion, microrobots were constructed using the PEG-based compounds 8-PEG-NH_2 and 8-PEG-NHS, which were chosen for their excellent biocompatibility and tunable mechanical properties (23). An adhesive peptide (RGD) was introduced to enhance MSC adhesion and proliferation on the microrobot surface. Moreover, phenylboronic acid groups were grafted onto the 8-PEG-NHS materials to scavenge excess ROS in the microenvironment to improve MSC survival. To construct microrobots that mimic magnetotactic bacteria, magnetic NP chains were formed within the hydrogel microspheres by directional assembly of the Fe_3O_4 NPs (*SI Appendix*, Fig. S2). Finite element simulation results indicated that single-chain arrangements of Fe_3O_4 NPs resulted in better retention than random and multichain arrangements, likely due to greater magnetic force generation (*SI Appendix*, Fig. S3). By controlling the solid content to 1.5%, we obtained single magnetic NP chain microrobots (Fig. 1*E*).

^{1}H nuclear magnetic resonance and X-ray photoelectron spectroscopy (XPS) confirmed the presence of the desired components and the grafting of boric acid groups (*SI Appendix*, Figs. S4 and S5). Their magnetization, assessed using an integrated physical property measurement system, showed superparamagnetic behavior with a saturation magnetization value of 15.4 emu g^{-1} (Fig. 1*F*), which can be precisely controlled under a programmable magnetic field. In addition, the Young's modulus decreased from 1,314 Pa to 514 Pa as the solid content decreased from 3% to 1.5% (Fig. 1*G* and *SI Appendix*, Fig. S6), illustrating the ultrasoft nature of the materials. These microrobots, which have superior softness and appropriate degradation time, are advantageous for navigating the complex vascular network of corpus cavernosum tissues (Fig. 1*H* and *SI Appendix*, Table S1), a significant improvement over traditional cell carrier.

To investigate the distribution of the microrobot in vivo, microcomputed tomography (μCT) and MRI (MRI) were used to observe the microrobot in the corpus cavernosum tissue. Owing to the high radiographic contrast between microrobots and tissues, μCT imaging clearly visualized the 3D spatial position of the microrobots in the corpus cavernosum tissue (*SI Appendix*, Fig. S7*A*). Importantly, the microrobots are evenly distributed in the corpus cavernosum tissue due to their ultrasoft (Fig. 1*I*). Moreover, the MRI results revealed that our microrobots had strong signal intensities, which correlated inversely with the Fe concentration (*SI Appendix*, Fig. S7*B*). Therefore, the distribution of microrobots in the corpus cavernosum can be precisely monitored by μCT or MRI in future clinical applications.

Controllable Motion of the Microrobot. The magnetic actuation of microrobots was realized by a Helmholtz coil and Maxwell coil electromagnetic drive system. Real-time visualization via an optical microscope and a closed-loop feedback module as a motion planner (*SI Appendix*, Fig. S8 *A* and *B*) demonstrated that the single chain microrobots had a greater motion speed (175 μm/s at 10 mT, 10 Hz) and a more accurate motion trajectory compared to the random and multichain arrangement of Fe_3O_4 NPs in the magnetic chain (*SI Appendix*, Fig. S8*C*). To clarify the mechanism by which the microrobots moved in a rotating magnetic field, we used 2D fluid models to simulate the propulsion of the microrobots (Fig. 2*A*). The direction of the magnetic dipole moment of the microrobot has consistently been attempting to align with the external magnetic field direction, thereby causing rotation of the microrobot. After the rotation of the microrobot, viscous frictional forces are generated at the interface, leading to rolling. This approach allowed precise navigation under a rotating magnetic field with a programmable circular trajectory (Fig. 2*B* and Movie S1).

The propulsion performance of the microrobots was also investigated in various biological fluids, which showed effective movement in DMEM, blood, and PBS (Fig. 2*C* and Movie S2). Speed dynamics in PBS were analyzed under different magnetic field intensities (2, 4, and 6 mT) and frequencies (1 to 40 Hz), identifying a linear increase in speed under maximum synchronized frequency, followed by a speed decrease due to fluidic drag exceeding the available magnetic torque (Fig. 2*D*). This loss of synchronization reduced the velocity, although increased magnetic field strength could enhance magnetic torque and increase motion speed. Furthermore, the ability of ultrasoft microrobots to navigate narrow blood vessels was investigated, demonstrating the ability of 135 μm microrobots to deform and pass through 100 μm tubes (Fig. 2*E* and Movie S3), unlike multiple NP chain microrobots (*SI Appendix*, Fig. S9). This softness is crucial for navigating the complex cavernous sinuses and preventing vascular damage. Magnetically driven upstream navigation against blood flow is essential for microrobots to perform a variety of tasks in vivo, especially in multivascular tissues such as the corpus cavernosum (24). We simulated a blood flow comparable to that of a capillary (500 μm/s) (25), and the microrobot could move upstream against the blood flow at a rate of 428 μm/s, indicating that the microrobots could perform controlled movements in a complex physiological environment (Fig. 2*F* and Movie S4).

We next tested whether the microrobots could be driven by a gradient magnetic field (*SI Appendix*, Fig. S10*A*). The gradient magnetic field could directly pull the microrobot to move with an average velocity of 184 μm/s along the gradient difference of the spatial magnetic field (*SI Appendix*, Fig. S10 *B* and *C*). In addition, the microrobot can be recognized in the ultrasound image despite the interference from the tissues, and control the movement well under the drive of the permanent magnet (*SI Appendix*, Fig. S10*D*).

The luminal diameters of various vessels in the corpus cavernosum, namely, the dorsal artery, artery branch, vein, and venule retrosinuses, are approximately 1.5 mm, 300 to 500 μm, 150 μm, and 30 μm, respectively (Fig. 2*G*). To assess the navigability of the microrobots in corpus cavernosum tissue, we investigated their movement within a 3D-printed microvascular network of the corpus cavernosum. The microrobot cluster, driven by a magnetic field, could be directed to broader areas, ensuring even distribution throughout the corpus cavernosum tissue and demonstrating excellent mobility (Fig. 2*H*).

Furthermore, we evaluated the retention ability of the microrobot in vitro. The microrobot could maintain its position in the microvasculature with the help of an external magnet (6.5 mm radius, 4 mm thickness), as shown in Fig. 2*I*. Removal of the magnet resulted in the microrobots being flushed away by blood flow (Movie S5). In addition, we tested whether magnetic-control equipment could enhance MSC-Rob retention in an ex vivo porcine corpus cavernosum model (*SI Appendix*, Fig. S11). The retention rate of the MSC-Rob increased from 40.60 to 84.70% with the aid of magnetic control at a simulated blood flow rate of 10 mL/min (Fig. 2*J*). Considering that human corpus cavernosum blood flow rates vary from 4 to 50 mL/min (26), the flow rate was adjusted to 4, 20, and 50 mL/min, yielding retention rates of up to 90.86%, 77.17%, and 68.78%, respectively (Fig. 2*K*). These results suggest that magnetic control significantly improves MSC retention in the ex vivo porcine corpus cavernosum.

To construct the optimal MSC-Rob, we first examined the hemocompatibility of the MSCs. Studies have shown that adverse thrombotic events induced by MSC therapy are associated with

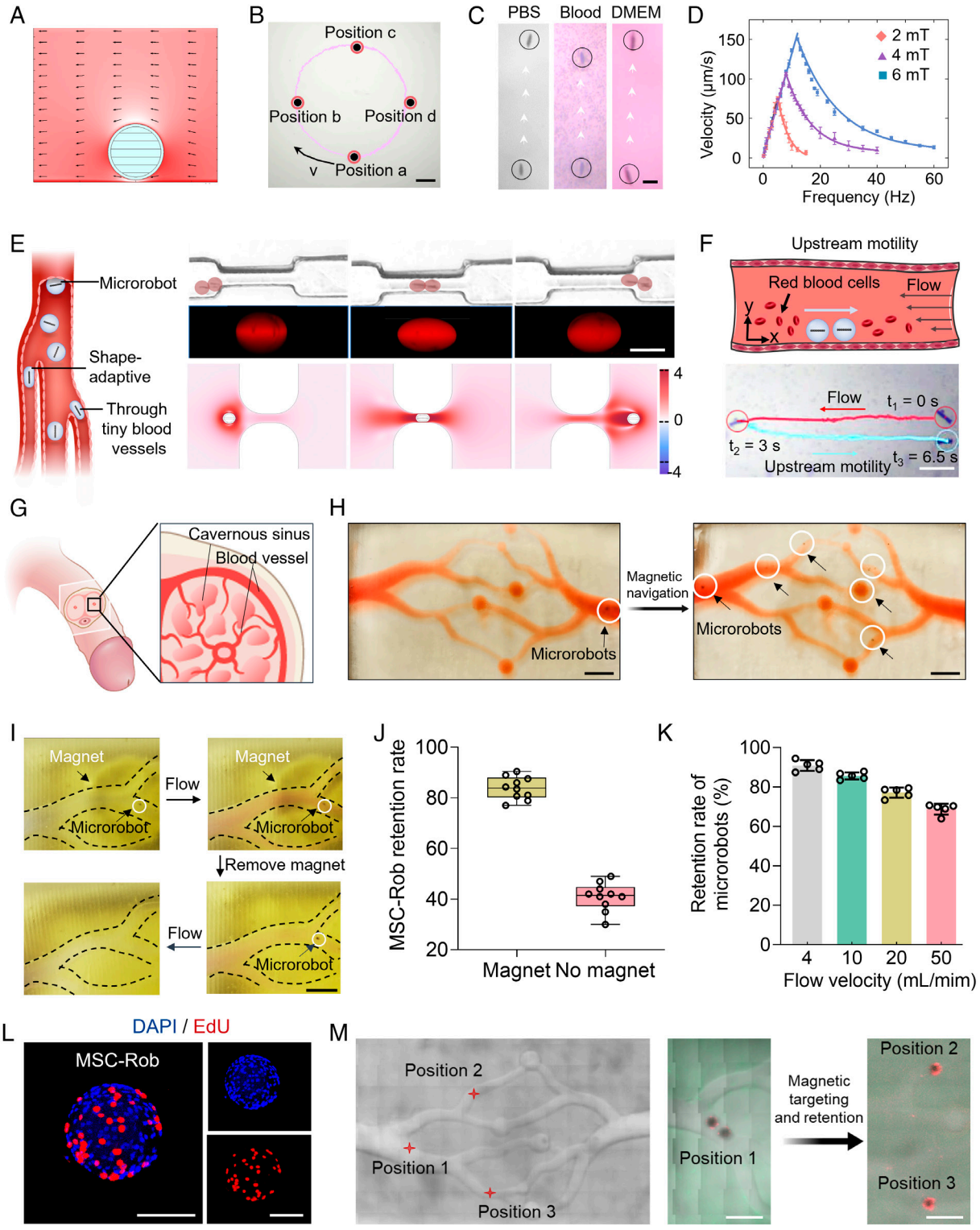

Fig. 2. Controllable microrobot motion in a magnetic field. (*A*) Finite element simulation of fluid flow around a clockwise-rotating microrobot. (*B*) Trajectories illustrating controllable magnetic propulsion of microrobots in a predefined circular trajectory under a rotating magnetic field (8 mT, 5 Hz). (Scale bar, 200 μm.) (*C*) Navigability of microrobots in various media under a rotating magnetic field (8 mT, 5 Hz). (Scale bar, 100 μm.) (*D*) Movement velocity of microrobots at different frequencies and magnetic field strengths (n = 3). (*E*) Optical and fluorescence microscopy images demonstrating the deformation of microrobots while passing through narrow gaps. (Scale bar, 200 μm.) Accompanied by finite element simulation of the deformation. (*F*) Time-lapse images showing controlled magnetic propulsion of microrobots upstream in blood flow. (Scale bar, 200 μm.) (*G*) Schematic illustration of the corpus cavernosum microvascular network. (*H*) Magnetic navigation of microrobots in a simple 3D-printed corpus cavernosum microvascular network. (*I*) Real-time imaging of microrobot retention with or without magnet. (*J*) Retention rate of MSC-Rob in an ex vivo porcine penis with or without magnet-assisted equipment at a simulated blood flow rate of 10 mL/min (n = 5 for each group). (*K*) Retention rate of the MSC-Robs at different flow rates. (n = 5 for each group). (*L*) MSC adhesion and proliferation on microrobots in the wells of low-adherence plates. Newly proliferating MSCs were detected by 5-ethynyl-2′-deoxyuridine (EdU) fluorescence staining (red). (Scale bar, 100 μm.) (*M*) Controlled locomotion and retention of the MSC-Rob over a low cell adhesion surface. (Scale bar, 500 μm.)

coagulation triggered by high procoagulant tissue factor (TF) expression in MSCs (27, 28). The tissue sources from which the MSCs were derived are probably the most important determinants of hemocompatibility, with bone marrow–derived MSCs showing lower TF expression and better hemocompatibility than adipose- or placental-derived MSCs (29) Additionally, TF expression is significantly lower at passage 3 (P3) than at passage 7 (*SI Appendix*, Fig. S12). Therefore, we selected P3 bone marrow–derived MSCs for all subsequent studies. We further examined the MSC loading efficiency, which proved successful after one day of coculture. MSCs adhered uniformly to the microrobots and proliferated normally, as evidenced by immunofluorescence analysis and SEM (Fig. 2*L* and *SI Appendix*, Fig. S13). The MSCs on the microrobot can spread and proliferate normally on the adhesive petri dish (*SI Appendix*, Fig. S14). These results confirm the noncytotoxic nature of the microrobots and their provision of a conducive environment for cell growth. The MSC-Rob can be navigated with high precision under a magnetic field in a simple microvascular network, and after anchoring by a magnet for approximately 12 h, the proliferation of the MSCs on microrobots occurs under low cell adhesion to microvessels at 37 °C (Fig. 2*M*).

We investigated the degradation of our microrobots in vitro and in vivo and found that they completely degraded within 180 d in vitro and 30 d in vivo (*SI Appendix*, Fig. S15 *A–D*). The iron oxide NPs within the microrobots travel through the bloodstream to the liver and spleen for metabolic processing. Biodistribution studies of these NPs in major organs showed no notable accumulation in the heart, liver, spleen, lungs, or kidneys, suggesting minimal side effects on these organs (*SI Appendix*, Fig. S15*F*). Additionally, fluorescence analyses of urine and feces indicated that the degradation products were excreted via urination (*SI Appendix*, Fig. S15*E*). Toxicity evaluations, including cytotoxicity data, blood biochemistry, and histology, revealed no evidence of harm within our tested dose and time range (*SI Appendix*, Fig. S16). Fertility impact assessments through semen analysis in rats showed no effect on semen concentration or motility (*SI Appendix*, Fig. S17). In addition, the MSC suspensions and the MSCs adhering to the microrobot presented weak expression of TF and did not significantly differ in terms of TF expression (*SI Appendix*, Fig. S18). We further performed hemocompatibility assessment by analyzing the coagulation marker data from the plasma of the MSC-injected and MSC-Rob rats and found no significant changes at one-month postinfusion (*SI Appendix*, Fig. S19). Therefore, major adverse thrombotic events were excluded. These findings collectively suggest that our MSC-Rob is relatively safe for clinical application.

MSC-Rob Improved the Retention and Survival of MSCs in Corpus Cavernosum Tissue. MSC-Rob was transplanted into the corpus cavernosum of rats and directed to distal vessels using a magnetic field. To enhance retention, rats were fitted with wearable equipment, including comfortable underwear with a permanent magnet (Fig. 3*A*). Despite the precise control of microrobots under rotating magnetic fields, the bulky size of current magnetic field generators and their inability to continuously operate limit user mobility. Thus, after initial targeting with rotating fields, a permanent magnet was used for sustained retention.

To assess in vivo retention efficiency, MSC-Rob and MSCs were injected into separate groups of rats. The rats wore magnetic equipment, allowing normal movement (Fig. 3*A* and *SI Appendix*, Fig. S20). Fourteen days later, the penile tissues of the MSC-Rob group exhibited strong fluorescence, while those of the MSC group exhibited negligible fluorescence (Fig. 3*B*). Dissection over seven days revealed that MSCs migrated to the lungs in the MSC group, whereas the MSC-Rob group retained most of the MSCs in the penis (Fig. 3*C*). Flow cytometry also revealed greater GFP-positive cell counts in the corpus cavernosum of the MSC-Rob group (Fig. 3*D*). These results confirmed that the MSC-Rob system could effectively enhance the retention of MSCs in the penis.

Gene Ontology (GO) analysis revealed that the up-regulated genes in ED model rats were related to oxidative stress (*SI Appendix*, Fig. S21*A*). High ROS levels in ED can cause senescence and apoptosis of transplanted MSCs, leading to repair failure (11, 30). To counter this, microrobots were equipped with phenylboronic acid groups for ROS scavenging. Coculture experiments demonstrated effective ROS elimination in MSCs cultured with microrobots, significantly reducing ROS levels compared to the control group (*SI Appendix*, Fig. S21 *B* and *C*). CCK8 assays and live-dead staining confirmed that ROS scavenging by microrobots increased MSC survival (*SI Appendix*, Fig. S21 *D* and *E*). Flow cytometry of penile tissues from ED model rats revealed that ROS levels decreased significantly after MSC-Rob treatment (Fig. 3*E*). These findings confirm that microrobots improve MSC survival by scavenging ROS in the corpus cavernosum.

MSC-Robs Promoted Repair of Corpus Cavernosum Tissue in ED Rats. After confirming the ability of the MSC-Rob system to enhance MSC survival and retention in the corpus cavernosum, we explored its therapeutic potential for treating ED in a rat model. We assessed the optimal injection dose of MSCs and MSC-Robs using the intracavernosal pressure-to-mean arterial pressure (ICP/MAP) ratio, a standard for evaluating penile erectile function in animals. We found that one million MSCs or 250 MSC-Robs could achieve the best ICP values, so we chose this injection dose for the subsequent experiments (*SI Appendix*, Fig. S22). We further investigated the therapeutic effects for ED one month after microrobot injection (*SI Appendix*, Fig. S23). The results revealed that there was no significant difference between the microrobot group and the ED model group, indicating that microrobots alone could not alleviate ED effectively.

One month after the administration of MSCs, MSC-Robs, or PBS to the different groups, we collected corpus cavernosum tissues. Masson's trichrome staining was performed to analyze tissue fibrosis, and the collagen-to-smooth muscle ratio was used as an indicator (Fig. 3*F*). Quantitative analysis revealed that the ratios of smooth muscle to collagen in the MSC-Rob and ED model groups were 19% and 3%, respectively, indicating that MSC-Rob administration significantly reduced fibrosis (Fig. 3*G*).

Penis erection is a delicate neurovascular process involving interactions between nerve cells, endothelial cells (ECs), and smooth muscle cells. We further examined the presence of the above cells by analyzing the expression of CD31, endothelial nitric oxide synthase (eNOS), neuronal nitric oxide synthase (nNOS), alpha-smooth muscle actin (α-SMA), and NF in corpus cavernosum tissue. Semiquantitative immunofluorescence analysis of the MSCs-Rob group revealed increased expression of smooth muscle and nerve markers compared to that in the ED and MSC groups (Fig. 3 *H* and *I*). Additional analysis of CD31, eNOS, and nNOS supported these findings (*SI Appendix*, Fig. S24), suggesting that MSC-Rob favors corpus cavernosum tissue repair. The ICP and MAP values were measured across groups (Fig. 3 *J* and *K*). The ICP/MAP ratio of the MSC-Rob group was 72.96 ± 8.72%, which was greater than that of the MSC group (59.22 ± 3.23%) and was almost as high as that of the control group (*SI Appendix*, Table S2). Doppler ultrasound assessment of blood flow in the corpus cavernosum revealed that MSC-Rob treatment increased the filling of the cavernous vascular sinuses (*SI Appendix*, Fig. S25 and Movie S6), indicating improved erectile function.

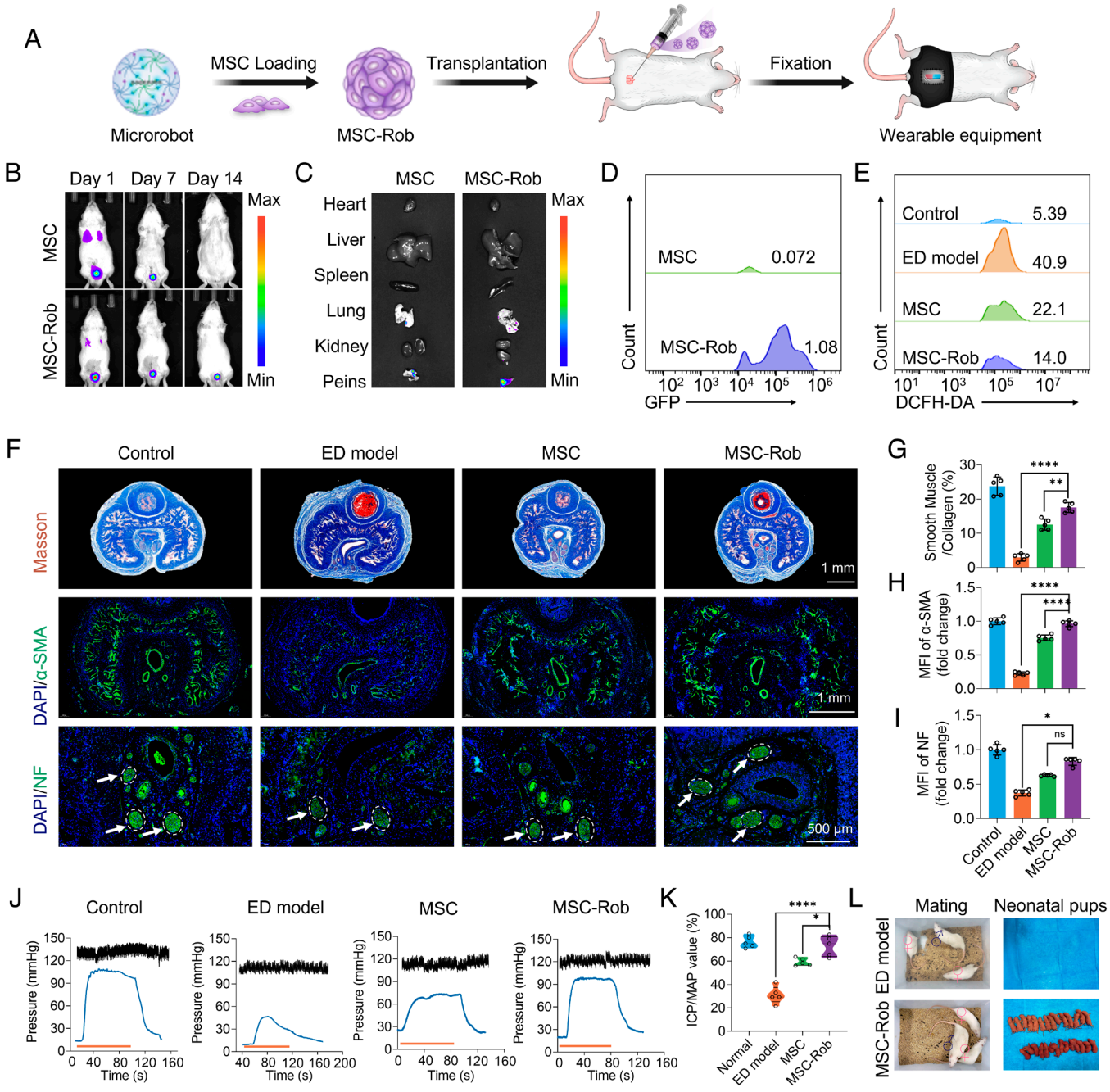

Fig. 3. MSC-Robs promoted corpus cavernosum repair in ED rats by improving the survival and retention of MSCs. (*A*) Schematic illustration of the process by which MSC-Rob was transplanted into the corpus cavernosum and guided to distal vessels by a magnetic field. (*B*) Fluorescence images of ED model rats post-MSC (MSC group) and MSC-Rob (MSC-Rob group) administration obtained with wearable magnetic equipment on days 1, 7, and 14. (*C*) Fluorescence-labeled MSC images of organs harvested from the MSC-Rob and MSC groups at 7 d. (Scale bar, 10 mm.)(*D*) Representative flow cytometry plots comparing the total number of GFP-MSCs in the MSC group and MSC-Rob group. (*E*) Representative flow cytometry plots showing the total intracellular ROS level in penis tissue. (*F*) Masson's trichrome staining and immunohistochemical staining of α-SMA and NF in penis tissue 30 d after ED in PBS-treated (ED model), MSC-treated, and MSC-Rob-treated corpus cavernosum samples. The control group represents the corpus cavernosum tissue of healthy rats; n = 5 per group. (*G–I*) Semiquantitative analysis of smooth muscle/collagen, α-SMA, and NF in the corpus cavernosum 30 d after ED treatment. (*J*) MAP and ICP oscillograms for the different groups. (*K*) The ICP/MAP ratio in the different groups; n = 5 per group. (*L*) Representative images of neonatal pups from the cage mating assay. $^{*}P < 0.05$, $^{***}P < 0.001$, and $^{****}P < 0.0001$. Statistical analysis was performed using one-way ANOVA with Tukey's correction (*G*, *H*, and *K*). Statistical analysis was performed using one-way ANOVA with Kruskal–Wallis correction (*I*).

ED can affect fertility. We conducted mating assays with male rats from different groups (control, ED model, MSC, and MSC-Rob) and two normal adult female rats (*SI Appendix*, Fig. S26*a*). All female rats that mated with the MSC-Rob group gave birth normally within the gestational cycle of 21 to 25 d, while only half did so after mating with the MSC group (Fig. 3*L* and *SI Appendix*, Fig. S26*b*), demonstrating that MSC-Rob effectively restored erection and fertility.

Cellular and Molecular Mechanisms of MSC-Rob in Promoting Corpus Cavernosum Tissue Repair. To elucidate the repair mechanism of MSC-Rob in corpus cavernosum tissue, we performed scRNA-seq analysis and identified eight major cell types (*SI Appendix*, Fig. S27 and Table S3). Given the critical role of ECs in mediating erectile function through their regulation of vasodilation, permeability, and growth factor production (31), we focused on the response of ECs to MSC-Rob treatment. We

categorized ECs into four subclusters (Fig. 4*A* and *SI Appendix*, Fig. S28). Notably, the EC-0 subcluster was significantly more prevalent in the MSC-Rob group, while the EC-1 subcluster was more common in the ED group. No significant differences were observed in the EC-2 and EC-3 subclusters between the two groups (Fig. 4*B*).

We conducted GO analysis to determine the function of each population of ECs based on the expression of the marker genes in each EC subcluster (Fig. 4*C*). The marker genes of the EC-0 subcluster were enriched in terms related to angiogenesis, such as "migration," "proliferation," and "regulation of vasculature development," indicating a correlation with corpus cavernosum tissue repair. In contrast, the marker genes of the EC-1 subcluster were linked to inflammatory and apoptotic processes, including "leukocyte cell–cell adhesion," "apoptosis," and "cellular response to chemical stress," indicating a relationship with cavernosal lesions. The marker genes of the EC-2 subcluster and EC-3 subcluster were related to angiogenesis, as they were related to wound healing, blood coagulation, muscle cell proliferation, and regulation of angiogenesis. Pathway analysis showed that EC proliferation and regulation of angiogenesis signaling pathway-related genes were mainly enriched in the EC-0 subcluster (Fig. 4 *D* and *E*), while genes related to the regulation of apoptotic signaling pathway-related genes were enriched mainly in the EC-1 subcluster (Fig. 4*F*). These findings suggest that MSC-Rob treatment effectively improved angiogenesis by increasing the regenerative EC-0 subcluster and decreasing the cavernosal lesion-related EC-1 subcluster. We further analyzed the secretome of MSCs and identified molecules that down-regulate endothelial inflammation and promote endothelial function (32–36), including THBS1, HDGF, GRN, PDGFD, VEGF, and GDF6 (*SI Appendix*, Fig. S29*A*). Importantly, the receptors corresponding to these molecules are expressed in the ECs of the corpora cavernosa (*SI Appendix*, Fig. S29*B*). These findings suggest that MSC-Rob may promote angiogenesis through the paracrine effects of MSCs.

The impact of MSC-Rob on Schwann cells (SCs), which are vital for nerve regeneration and axonal growth, was also examined (37) (Fig. 4*G*). In the MSC-Rob group, pathways related to neurogenesis, such as axon guidance and AMPK signaling, were up-regulated, as were pro-nerve repair genes, such as Nrep, Nptn, and Nbeal1 (Fig. 4*H* and *SI Appendix*, Fig. S30). The expression of inflammatory cytokine-producing genes, such as Ccl2, was down-regulated in SCs from the MSC-Rob group (*SI Appendix*, Fig. S30). Additionally, the Hedgehog signaling pathway, which is crucial for nervous system healing postinjury (38), was more active in the MSC-Rob group than in the ED group.

The immune system is closely associated with tissue damage and regeneration, and its effective regulation is essential for tissue regeneration (39). GO enrichment analysis of the up-regulated differentially expressed genes (DEGs) in immune cells revealed enrichment in terms such as "leukocyte chemotaxis" and "macrophage activation" in the ED group (*SI Appendix*, Fig. S31). After the administration of MSC-Rob, the above signaling pathways were down-regulated (*SI Appendix*, Fig. S32). We further identified six subclusters (Fig. 4*I* and *SI Appendix*, Fig. S33 and Table S4). Macrophages, the most abundant immune cells, are categorized as inflammatory or regenerative based on the expression of markers such as IL-1β and CD206 (Fig. 4 *J* and *K*). Notably, MSC-Rob treatment significantly increased the proportion of regenerative macrophages and decreased the proportion of inflammatory macrophages (Fig. 4 *L* and *M*). Immunofluorescence staining corroborated these findings, revealing an increase in regenerative macrophages and a decrease in inflammatory macrophages post-treatment (*SI Appendix*, Fig. S34). Furthermore, GO enrichment analysis demonstrated that MSC-Rob treatment increased oxidative phosphorylation and the mitochondrial membrane potential in macrophages. Mitochondrial membrane potential measurements confirmed that MSC-Rob significantly restored the mitochondrial function in macrophages (*SI Appendix*, Fig. S35).

Macrophages play vital roles in angiogenesis and neurogenesis through interactions with ECs and SCs (39, 40). CellPhone DB analysis revealed a decrease in proinflammatory signaling (e.g., CXCL13–ACKR4 and IL1B–ADRB2 interactions between macrophages and ECs) and an increase in prorepair signaling (e.g., TGFB1–TGFBR3 interactions between macrophages, ECs, and SCs) in the MSC–Rob group compared with the ED model group (Fig. 4*N*). These results suggest that MSC-Rob treatment actively promotes EC and SC repair by modulating macrophage function (Fig. 4*O*).

MSC-Rob Assisted in Restoring Erectile Function in a Beagle ED Model. We examined whether MSC-Rob could restore erectile function in beagles with ED by injecting MSC-Rob into penile tissue (Fig. 5*A*). Doppler ultrasound revealed enhanced blood flow and an increased cavernous sinus diameter in the MSC-Rob group (Fig. 5*B*). Additionally, the MAP and ICP were evaluated upon cavernous nerve stimulation (*SI Appendix*, Fig. S36 *A* and *B*). The ICP/MAP ratio in the MSC-Rob group (72 ± 0.86%) was significantly higher than that in the ED model group (42 ± 3.4%) and MSC group (59.8 ± 2.4%), indicating improved erectile function (Fig. 5*C*).

Histological analysis using Masson and immunofluorescence staining was also conducted. Masson staining revealed a greater muscle and collagen proportion in the MSC-Rob group than in the ED model and MSC groups (*SI Appendix*, Fig. S36*C*), which is consistent with the results observed in rats. Immunofluorescence staining indicated significantly greater levels of α-SMA and NF in the MSC-Rob group than in the control group (Fig. 5*D*). RT–qPCR further confirmed the elevated gene expression of endothelial, nerve, and smooth muscle markers in the MSC-Rob group (*SI Appendix*, Table S5 and Fig. S36 *D–F*), suggesting effective restoration of corpus cavernosum tissue. To assess fertility, one male beagle from each group (control, ED model, MSC, and MSC-Rob) was mated with two normal adult female beagles (Fig. 5*E*). During the 58-to-65-d gestational cycle, 83% of the female beagles that mated with the MSC-Rob group had successful pregnancies and births, while none of the females that mated with the ED group conceived, demonstrating the efficacy of MSC-Rob in restoring erectile function and fertility (Fig. 5 *F* and *G* and *SI Appendix*, Fig. S37).

Discussion

MSCs have shown promise in treating refractory ED, such as neurological and diabetic ED, in clinical studies. However, direct injection into the corpus cavernosum alone has limitations; a clinical study reported less than 40% recovery in ED patients after MSC treatment (41). This limited success is attributed to poor cell retention in the corpus cavernosum due to unique hemodynamics, leading to rapid loss of transplanted cells and a hostile microenvironment causing senescence or apoptosis in transplanted MSCs (11, 42, 43). Magnetic microrobots, which provide targeted transport and retention of MSCs via magnetic force, offer promising applications in disease treatment (21, 44). However, scaling up experiments with magnetic actuation from small animals, such as mice, to humans may require a penetration depth increase of one order of magnitude (45). Notably, the ED, which is a superficial and organ-related condition, is more responsive to external magnetic fields than other diseases, facilitating clinical translation.

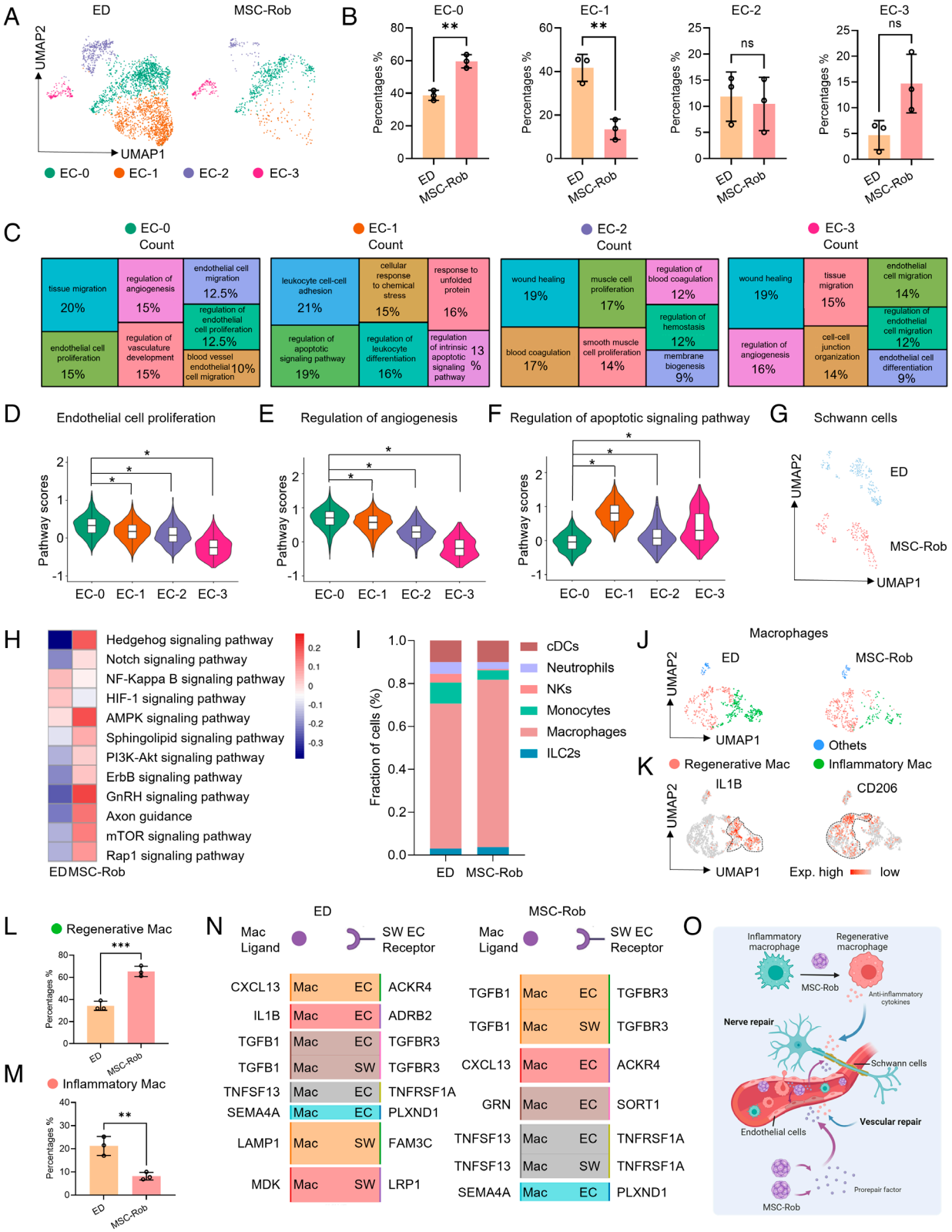

Fig. 4. Cellular and molecular mechanisms by which MSC-Rob promotes the repair of damaged nerves and blood vessels. (*A*) UMAP plots of the four endothelial cell (EC) subclusters in the ED and MSC-Rob groups. (*B*) Bar plot showing the distribution of each EC subcluster in the ED and MSC-Rob groups. (*C*) Gene Ontology (GO) analysis for each EC subcluster transition, with the box size representing the number of significant terms in each GO category. (*D–F*) Combined violin and box plots displaying the expression levels of genes related to EC proliferation, regulation of angiogenesis, and regulation of apoptotic pathways in EC subclusters by the Wilcoxon rank-sum test. (*G*) UMAP plots of the Schwann cell subclusters in the ED and MSC-Rob groups. (*H*) Heatmap presenting the top pathways associated with genes whose expression was activated or inhibited in Schwann cells from the ED model and MSC-Rob groups based on the GSVA of DEGs. (*I*) Bar plot showing the distribution of each immune cell subcluster in the groups. (*J* and *K*) UMAP plots of the three macrophage subclusters in the ED and MSC-Rob groups, colored according to cell type or classic marker gene expression level. (*L* and *M*) Bar plots indicating the percentages of regenerative and inflammatory macrophage subclusters in the ED and MSC-Rob groups. (*N*) Alluvial plot showing significant ligand–receptor pairs in the ED and MSC-Rob groups, as identified by NicheNetR analysis. This analysis considered only macrophage (ligand) interactions with SCs and ECs, including interactions between differentially expressed ligands and receptors ($P < 0.05$). (*O*) A mechanistic summary illustrating how MSC-Rob promotes recovery of the corpus cavernosum. *$P < 0.05$, ***$P < 0.001$, ****$P < 0.0001$. Statistical analysis was performed using two-tailed Student's *t* tests (*B*, *L*, and *M*).

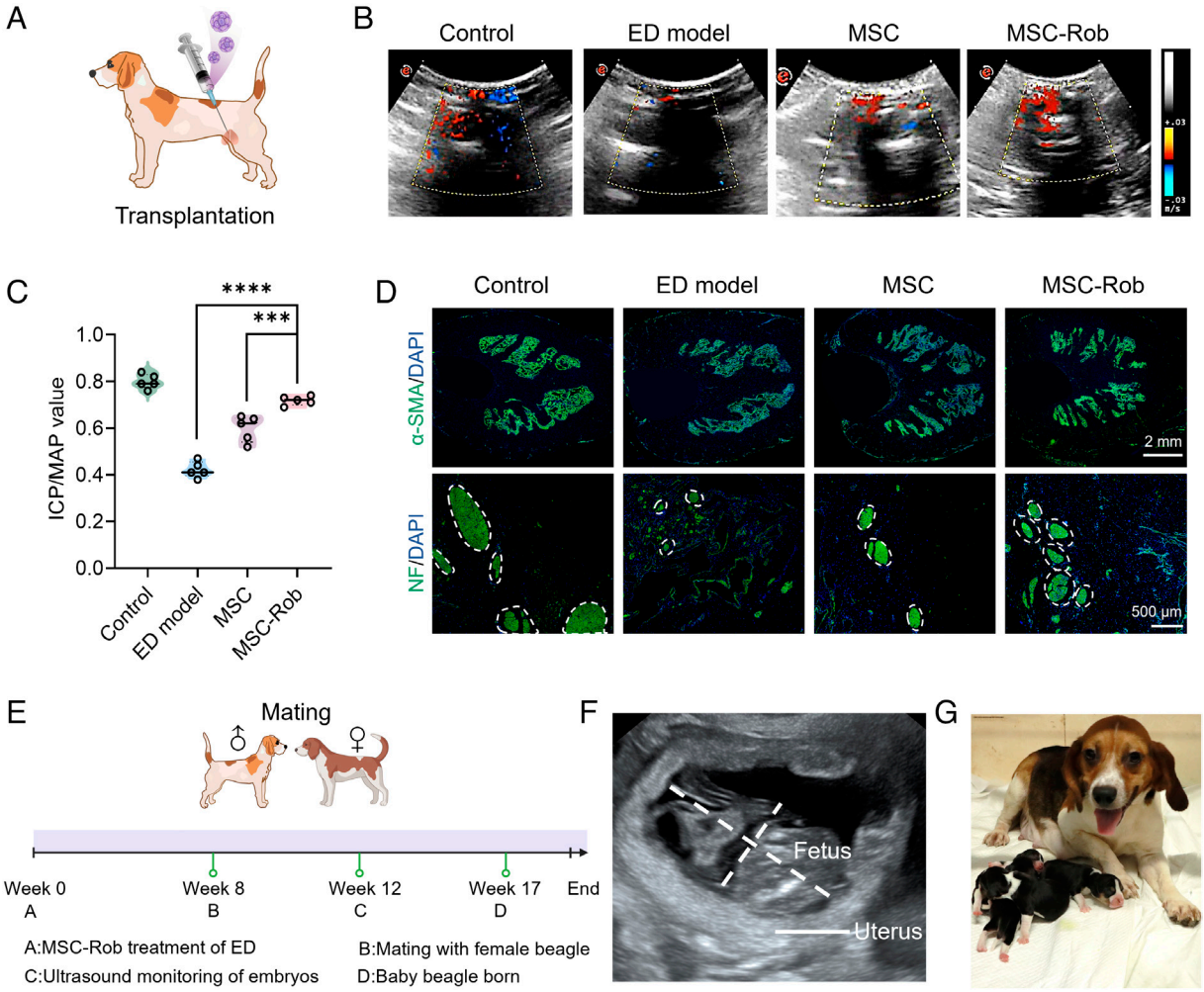

Fig. 5. MSC-Rob restored erectile function in a beagle model of ED. (*A*) Illustration of MSC-Rob transplantation into the corpus cavernosum of beagle models with ED. (*B*) Color Doppler sonography was used to assess blood flow in corpus cavernosum tissue 8 wk after ED induction with PBS (ED model) and following MSC or MSC-Rob treatment and control (normal) group. Red and blue, along with brightness, represent the blood flow direction and velocity, respectively. (*C*) Comparison of the ICP to MAP ratio among the different groups (n = 5 per group). (*D*) Fluorescence immunostaining of α-SMA and NF in the corpus cavernosum 8 wk after different groups. (*E*) Schematic of the fertility test procedure using a cage mating assay with one male and two female beagles. (*F*) Ultrasound images of fetuses following the mating of male beagles post-MSC-Rob treatment with normal female beagles. (*G*) Representative images of beagle puppies born from these mattings. ***$P < 0.001$ and ****$P < 0.0001$. Statistical analysis was performed using one-way ANOVA with Tukey's correction (*C*).

Our ultrasoft magnetic microrobot was designed to improve the retention and survival of MSCs and enhance the biological function of MSCs in ED treatment. The use of microrobots for delivering cells or drugs to enhance their therapeutic effects has been studied in other types of tissue repair, such as bone and nerve tissue (46, 47). For example, PLGA microrobots delivering MSCs can effectively promote cartilage regeneration (21). Learning from the work of pioneers, we have better designed and optimized microrobots for ED therapy. The proposed MSC-Rob in this study features favorable biocompatibility and simple preparation methods. Its softness, with a Young's modulus similar to that of human adipose tissue (1 kPa; Fig. 1 *G* and *H*), is one of the ultrasoft microrobots reported for cell delivery thus far (*SI Appendix*, Table S1). This feature makes the microrobots highly adaptable, preventing blood vessel blockage.

The retention of MSCs-Rob in the corpus cavernosum for more than 14 d was more than double that of MSCs injected alone (Fig. 3 *B*–*D*). In addition, our microrobots could also effectively remove ROS via hydrolysis of the borate ester bond (48), improving the survival rate of MSCs (Fig. 3*E* and *SI Appendix*, Fig. S21). Moreover, MSC-Rob treatment led to ICP/MAP values comparable to those of control animals, indicating successful restoration of erectile function (Figs. 3 and 5).

Previous studies have shown that the repair and homeostasis maintenance functions of MSCs rely on their interaction with the inflammatory microenvironment (49, 50). However, the specific mechanisms by which MSCs influence the corpus cavernosum microenvironment remain unclear. Our research sheds light on the cellular composition, biological characteristics, and regulatory signaling networks within the corpus cavernosum, enhancing our understanding of how MSC-Rob expedites tissue repair (Fig. 4). We found that MSC-Rob treatment effectively promoted angiogenesis and neurogenesis. This effect is achieved by increasing the presence of regenerative endothelial subclusters while reducing those associated with cavernosal lesions. MSC-Rob treatment also modulates signaling between cells by reducing proinflammatory interactions between macrophages and ECs and enhancing prorepair signaling involving macrophages, ECs, and SCs (Fig. 4). On the other hand, MSCs directly promote blood vessel repair

through paracrine effects. Although we detected the expression of several MSC-secreted factor receptors in ECs (*SI Appendix*, Fig. S29), the specific roles of these molecules in ED treatment require further investigation. Modifying MSCs by overexpressing beneficial mediators, such as VEGF, may be an effective way to further improve clinical efficacy, which will be the focus of our future research.

In vivo safety assessments confirmed that MSC-Rob injection did not cause major organ damage, loss of sperm quality, or clot formation or thromboembolic events (*SI Appendix*, Fig. S16–S19). The microrobot is composed of Fe_3O_4 NPs and cross-linked PEG microspheres. Fe_3O_4 NPs have been classified as biofriendly and can be metabolized by the kidneys without obvious toxicity (51). In addition, PEG microspheres are biocompatible, degradable, and have been approved by the FDA (*SI Appendix*, Fig. S15). Studies have shown that thromboembolic complications are most commonly associated with the infusion of MSC products with high procoagulant TF expression (27, 28). For safety, MSC TF expression should be tested first when using MSCs and MSC-Rob to confirm that it is within the safe range. When MSCs with high TF expression or high doses are applied, further processing (such as anticoagulation) should be taken to reduce the risk of coagulation reactions.

In summary, our work is an important step toward advancing the clinical application of MSCs for ED treatment. This study reports the use of microrobots for ED treatment and demonstrates their ability to restore erectile function in ED models of rats and beagles. While our MSC-Rob system shows promise for the treatment of ED, there are still some issues that need to be improved or developed before it can be applied in future clinical trials. First, a more ergonomic and convenient patch with a magnet array should be designed to achieve precise control of the position within the corpus cavernosum of the microrobots to better improve the retention of the MSC. Second, the reported MSC-Rob needs careful formulation optimization. Finally, this study focused on short-term effects and had a small sample size, and future studies could extend the observation time and expand the sample size to evaluate long-term efficacy and potential side effects.

Materials and Methods

Detailed methods are found in *SI Appendix*.

Materials. 8-PEG-NHS and 8-PEG-NH_2 were purchased from Sinopeg. $FeCl_3$ $6H_2O$, sodium oleate, ethyl alcohol, hexane, oleic acid, 1-octadecene, liquid paraffin, and 3-aminomethylphenylboronic acid hydrochloride were obtained from Shanghai Macklin Biochemical Co., Ltd. TenX phosphate-buffered saline (PBS), RPMI 1640 medium, and DMEM were purchased from Thermo Fisher Scientific Co., Ltd. Cell Counting Kit-8 (CCK-8), a highly sensitive DCFH-DA ROS assay kit, and calcein-AM/propidium iodide (PI) were purchased from Dojindo Chemical Technology (Shanghai) Co., Ltd.

Microrobot Preparation. The microrobots were prepared via a straightforward emulsification method. First, 3-aminomethylphenylboronic acid hydrochloride (2 mg), RGD peptide (2 mg), and 8-PEG-NHS (15 mg) were dissolved in 50 μl of dimethyl sulfoxide (DMSO), and the mixture was added to 8-PEG-NH_2 (15 mg) and Fe_3O_4 NPs (15 mg) dissolved in 2 ml of PBS to form a uniform water phase. The water phase was added to an oil solution composed of liquid paraffin and Span 80, and the mixture was stirred for 30 min at room temperature. The resulting microrobots were washed five times with PBS. The samples were stored at 4 °C.

To control the configuration of magnetic NPs, managing the solid content is essential. By setting the solid content of 8-PEG-NH_2 and 8-PEG-NHS at 1.5%, we fabricated microrobots consisting of single chains of magnetic NPs. Increasing the solid content to 2% enabled the creation of microrobots with multiple magnetic NP chains. At a solid content of 3%, the result was the formation of microrobots with random arrangements of magnetic NPs.

Ethics Statement

All animal surgeries were reviewed and approved by the Animal Ethical and Welfare Committee of Guangzhou Shuiyuntian Biotechnology Co., Ltd. (Guangzhou, China) or the Animal Ethical and Welfare Committee of Guangdong Laidi Biomedical Research Institute Co, Ltd. (Guangzhou, China) and followed the Guidelines for the Care and Use of Laboratory Animals of the NIH; permit numbers 2023044-1, SYT2023133, and SYT2024051. Additionally, this study was conducted following the ARRIVE guidelines for the use of animals in experimentation. Rat bone marrow MSCs and beagle bone marrow MSCs were purchased from Cyagen Biosciences (Guangzhou) Inc.

Preparation of a Single-Cell Suspension of Corpus Cavernosum Tissue. Corpus cavernosum tissue was obtained from the control, ED model, and MSC-Rob groups and washed three times with Hanks' balanced salt solution (HBSS). Subsequently, the tissues were cut to 1 to 2 mm in size and sterilized with 2 ml of GEXSCOPE^{TM} tissue dissociation solution (Singleron) for 15 min at 37 °C. After digestion, the samples were filtered through a 40-micron sterile strainer, the filtrate was centrifuged at 215×g for 5 min, the supernatant was discarded, and the cells were resuspended in 1 ml of PBS. Two milliliters of GEXSCOPE^{TM} erythrocyte lysis buffer (Singleron) were added, and the cells were incubated for 10 min at 25 °C. The cell suspension was centrifuged at 500×g for 5 min and resuspended in 1 ml of PBS. The resuspended cell suspension was incubated with 0.5% Trypan blue (Sigma) for 3 min at room temperature, and cell viability was evaluated by counting the number of live and dead cells under a microscope (52, 53).

Evaluation of Erectile Function. Under anesthesia, the rats were restrained with a rat fixator, and the cavernous nerve, corpus cavernosum, and carotid artery were exposed. Two catheters containing heparin sodium solution (50 IU) were inserted into the carotid artery for continuous monitoring of the MAP and the corpus cavernosum for continuous monitoring of the ICP, and the cavernous nerve was stimulated. The stimulation time was 60 s at 5 V, 25 Hz, and 2 ms. For the beagle, two catheters containing heparin sodium solution (50 IU) were inserted into the femoral artery for continuous monitoring of the MAP and the corpus cavernosum for continuous monitoring of the ICP, and the cavernous nerve was stimulated. The stimulation time was 60 s at 2 V, 2 ms, and 20 Hz. The ratio of the ICP to the MAP was used to evaluate erectile function. The data were visualized via a BL420F biological signal recording and analysis system (Techman Software Co., Ltd., Chengdu, China).

Statistical Analysis. Sample sizes were determined on the basis of the authors' experience with the preliminary studies and by referencing a study on erectile function recovery with 80% power ($\alpha = 0.05$) (54–56). All the data are expressed as the means ± SD. GraphPad Prism 7.0 software was used for the statistical analysis. The datasets were tested for normality with Shapiro–Wilk tests. For normally distributed data, we applied parametric statistics. Two-tailed Student's *t* tests or one-way ANOVA were used for analyzing experimental setups requiring the testing of two conditions or more than two conditions, respectively. *P* values were corrected for multiple testing according to Tukey tests. In cases where the data did not meet the assumptions for parametric tests, one-way ANOVA with Kruskal–Wallis correction was conducted for nonnormally distributed data. These nonparametric methods were chosen on the basis of the data characteristics and

to ensure the robustness and validity of our statistical analyses. *P*-values are denoted as $^{*}P < 0.05$, $^{**}P < 0.01$, $^{***}P < 0.001$, and $^{****}P < 0.0001$, and *P* values > 0.05 were considered to represent statistically significant differences.

Data, Materials, and Software Availability. scRNA-seq datasets used in this study have been deposited in the Sequence Read Archive and are available under accession number PRJNA1172004 (57).

ACKNOWLEDGMENTS. This work was financially supported by the National Natural Science Foundation of China (T2288101 and U22A20157), the Natural Science Foundation for Outstanding Youth Team Project of Guangdong Province (2024B1515040030), and the Guangdong Basic and Applied Basic Research Foundation Outstanding Youth Project (2021B1515020064).

Author affiliations: [a]National Engineering Research Centre for Tissue Restoration and Reconstruction, South China University of Technology, Guangzhou 510006, P. R. China; [b]School of Materials Science and Engineering, South China University of Technology, Guangzhou 510640, P. R. China; [c]Key Laboratory of Biomedical Engineering of Guangdong Province, South China University of Technology, Guangzhou 510006, P. R. China; [d]Department of Urology, Shandong Provincial Hospital Affiliated to Shandong First Medical University, Jinan 250021, P. R. China; [e]Hospital of Stomatology, Guanghua School of Stomatology, Sun Yat-sen University, Guangzhou 510055, P. R. China; [f]Department of Andrology, The First Affiliated Hospital, Sun Yat-sen University, Guangzhou 510080, P. R. China; [g]School of Materials Science and Engineering, Harbin Institute of Technology, Shenzhen 518071, P. R. China; [h]School of Materials Science and Engineering, Dongguan University of Technology, Dongguan 523808, P. R. China; [i]Institute of Biomaterials and Bioengineering, Tokyo Medical and Dental University, Chiyoda-ku 113-8510, Tokyo, Japan; [j]Department of Chemistry, The Hong Kong University of Science and Technology, Hong Kong 999077, P. R. China; [k]School of Biomedical Sciences and Engineering, South China University of Technology, Guangzhou International Campus, Guangzhou 511442, P. R. China; [l]Department of Biomedical Engineering Columbia University, New York, NY 10032; and [m]Reproductive Centre The Sixth Affiliated Hospital Sun Yat-sen University, Guangzhou 510655, P. R. China

1. F. A. Yafi *et al.*, Erectile dysfunction. *Nat. Rev. Dis. Primers.* **2**, 16003 (2016).
2. R. Shamloul, H. Ghanem, Erectile dysfunction. *The Lancet* **381**, 153–165 (2013).
3. M. Ji *et al.*, The role of mechano-regulated YAP/TAZ in erectile dysfunction. *Nat. Commun.* **14**, 3758 (2023).
4. E. Llorens-Bobadilla *et al.*, A latent lineage potential in resident neural stem cells enables spinal cord repair. *Science* **370**, eabb8795 (2020).
5. S. Golpanian, A. Wolf, K. E. Hatzistergos, J. M. Hare, Rebuilding the damaged heart: Mesenchymal stem cells, cell-based therapy, and engineered heart tissue. *Physiol. Rev.* **96**, 1127–1168 (2016).
6. R. Zhu *et al.*, Mesenchymal stem cell treatment improves outcome of COVID-19 patients via multiple immunomodulatory mechanisms. *Cell. Res.* **31**, 1244–1262 (2021).
7. D. Z. Sun, B. Abelson, P. Babbar, M. S. Damaser, Harnessing the mesenchymal stem cell secretome for regenerative urology. *Nat. Rev. Urol.* **16**, 363–375 (2019).
8. D. M. Hoang *et al.*, Stem cell-based therapy for human diseases. *Signal Transduct. Tar.* **7**, 272 (2022).
9. G. Chen *et al.*, Roe-inspired stem cell microcapsules for inflammatory bowel disease treatment. *Proc. Natl. Acad. Sci. U.S.A.* **118**, e2112704118 (2021).
10. B. N. Kharbikar, P. Mohindra, T. A. Desai, Biomaterials to enhance stem cell transplantation. *Cell Stem. Cell* **29**, 692–721 (2022).
11. P. Chen, Z. Chen, J. Zhai, W. Yang, H. Wei, Overexpression of PRDX2 in adipose-derived mesenchymal stem cells enhances the therapeutic effect in a neurogenic erectile dysfunction rat model by inhibiting ferroptosis. *Oxid. Med. Cell. Longev.* **2023**, 4952857 (2023).
12. T. Wang *et al.*, Clinical translation of wireless soft robotic medical devices. *Nat. Rev. Bioeng.* **2**, 470–485 (2024).
13. X. Wang *et al.*, Colloidal tubular microrobots for cargo transport and compression. *Proc. Natl. Acad. Sci. U.S.A.* **120**, e2304685120 (2023).
14. C. Simó *et al.*, Urease-powered nanobots for radionuclide bladder cancer therapy. *Nat. Nanotechnol.* **19**, 554–564 (2024).
15. S. Liu *et al.*, Treatment of infarcted heart tissue via the capture and local delivery of circulating exosomes through antibody-conjugated magnetic nanoparticles. *Nat. Biomed. Eng.* **4**, 1063–1075 (2020).
16. F. Zhang *et al.*, Nanoparticle-modified microrobots for in vivo antibiotic delivery to treat acute bacterial pneumonia. *Nat. Mater.* **21**, 1324–1332 (2022).
17. B. J. Nelson, S. Pané, Delivering drugs with microrobots. *Science* **382**, 1120–1122 (2023).
18. B. Wang *et al.*, Endoscopy-assisted magnetic navigation of biohybrid soft microrobots with rapid endoluminal delivery and imaging. *Sci. Robot.* **6**, eabd2813 (2021).
19. N. Li *et al.*, Human-scale navigation of magnetic microrobots in hepatic arteries. *Sci. Robot.* **9**, eadh8702 (2024).
20. W. Chen *et al.*, Recent progress of micro/nanorobots for cell delivery and manipulation. *Adv. Funct. Mater.* **32**, 2110625 (2022).
21. G. Go *et al.*, Human adipose–derived mesenchymal stem cell–based medical microrobot system for knee cartilage regeneration in vivo. *Sci. Robot.* **5**, eaay6626 (2020).
22. X.-Z. Chen *et al.*, Magnetically driven piezoelectric soft microswimmers for neuron-like cell delivery and neuronal differentiation. *Mater. Horiz.* **6**, 1512–1516 (2019).
23. Y. Bu *et al.*, Tetra-PEG based hydrogel sealants for in vivo visceral hemostasis. *Adv. Mater.* **31**, 1901580 (2019).
24. Y. Qiu, D. R. Myers, W. A. Lam, The biophysics and mechanics of blood from a materials perspective. *Nat. Rev. Mater.* **4**, 294–311 (2019).
25. H. Zhang *et al.*, Dual-responsive biohybrid neutrobots for active target delivery. *Sci. Robot.* **6**, eaaz9519 (2021).
26. U. Wetterauer, "Anatomy of the penis and physiology of erection" in *Sexology* (Springer, 1988), pp. 115–126.
27. M. Guido *et al.*, Intravascular mesenchymal stromal/stem cell therapy product diversification: Time for new clinical guidelines. *Trends Mol Med.* **25**, 149–163 (2019).
28. M. Guido *et al.*, Improved MSC minimal criteria to maximize patient safety: A call to embrace tissue factor and hemocompatibility assessment of MSC products. *Stem. Cells Transl. Med.* **11**, 2–13 (2022).
29. M. Guido *et al.*, Different procoagulant activity of therapeutic mesenchymal stromal cells derived from bone marrow and placental decidua. *Stem Cells Dev.* **24**, 2269–79 (2015).
30. C. Holze *et al.*, Oxeiptosis, a ROS-induced caspase-independent apoptosis-like cell-death pathway. *Nat. Immunol.* **19**, 130–140 (2018).
31. L. Zhao *et al.*, Single-cell transcriptome atlas of the human corpus cavernosum. *Nat. Commun.* **13**, 4302 (2022).
32. H.-W. Chiu *et al.*, Nattokinase attenuates endothelial inflammation through the activation of SRF and THBS1. *Int. J. Biol. Macromol.* **268**, 131779 (2024).
33. E. Hirayuki *et al.*, Hepatoma-derived growth factor: An overview and its role as a potential therapeutic target molecule for digestive malignancies. *Int. J. Mol. Sci.* **13**, 4216 (2020).
34. P. S. Bansal *et al.*, Development of a potent wound healing agent based on the liver fluke granulin structural fold. *J. Med. Chem.* **60**, 4258–4266 (2017).
35. M. Bernard *et al.*, Endothelial PDGF-D contributes to neurovascular protection after ischemic stroke by rescuing pericyte functions. *Cell Mol. Life Sci.* **81**, 225 (2024).
36. R. Wu *et al.*, A novel human long noncoding RNA SCDAL promotes angiogenesis through SNF5-mediated GDF6 expression. *Adv. Sci.* **8**, e2004629 (2021).
37. R. Stavely *et al.*, Schwann cells in the subcutaneous adipose tissue have neurogenic potential and can be used for regenerative therapies. *Sci. Transl. Med.* **14**, eabl8753 (2022).
38. Y.-D. Zhang *et al.*, Lentivirus-mediated silencing of the PTC1 and PTC2 genes promotes recovery from spinal cord injury by activating the Hedgehog signaling pathway in a rat model. *Exp. Mol. Med.* **49**, e412 (2017).
39. T. Lazarov, S. Juarez-Carreño, N. Cox, F. Geissmann, Physiology and diseases of tissue-resident macrophages. *Nature* **618**, 698–707 (2023).
40. J. Li *et al.*, Modulation of the crosstalk between Schwann cells and macrophages for nerve regeneration: A therapeutic strategy based on a multifunctional tetrahedral framework nucleic acids system. *Adv. Mater.* **34**, 2202513 (2022).
41. J. A. Levy, M. Marchand, L. Iorio, W. Cassini, M. P. Zahalsky, Determining the feasibility of managing erectile dysfunction in humans with placental-derived stem cells. *J. Osteopath. Med.* **116**, e1–e5 (2016).
42. Q. Tian *et al.*, Multifaceted catalytic ROS-scavenging via electronic modulated metal oxides for regulating stem cell fate. *Adv. Mater.* **34**, 2207275 (2022).
43. X. C. Jiang *et al.*, Neural stem cells transfected with reactive oxygen species–responsive polyplexes for effective treatment of ischemic stroke. *Adv. Mater.* **31**, 1807591 (2019).
44. F. Soto, J. Wang, R. Ahmed, U. Demirci, Medical micro/nanorobots in precision medicine. *Adv. Sci.* **7**, 2002203 (2020).
45. R. Nauber *et al.*, Medical microrobots in reproductive medicine from the bench to the clinic. *Nat. Commun.* **14**, 728 (2023).
46. S. Jeon *et al.*, Magnetically actuated microrobots as a platform for stem cell transplantation. *Sci. Robot.* **4**, eaav4317 (2019).
47. G. Go *et al.*, A magnetically actuated microscaffold containing mesenchymal stem cells for articular cartilage repair. *Adv. Healthc. Mater.* **6**, 1601378 (2017).
48. C. Wang *et al.*, In situ formed reactive oxygen species–responsive scaffold with gemcitabine and checkpoint inhibitor for combination therapy. *Sci. Transl. Med.* **10**, eaan3682 (2018).
49. S. Naik, S. B. Larsen, C. J. Cowley, E. Fuchs, Two to tango: Dialog between immunity and stem cells in health and disease. *Cell* **175**, 908–920 (2018).
50. T. J. Rabelink, M. H. Little, Stromal cells in tissue homeostasis: Balancing regeneration and fibrosis. *Nat. Rev. Nephrol.* **9**, 747–753 (2013).
51. H. H. Gustafson *et al.*, Nanoparticle uptake: The phagocyte problem. *Nano Today.* **10**, 487–510 (2015).
52. Z. Shen *et al.*, The spatial transcriptomic landscape of human gingiva in health and periodontitis. *Sci. China Life Sci.* **67**, 720–732 (2024).
53. Z. Shen *et al.*, Restoring periodontal tissue homoeostasis prevents cognitive decline by reducing the number of Serpina3nhigh astrocytes in the hippocampus. *Innovation.* **5**, 100547 (2023).
54. A. A. Kathleen *et al.*, Clarifying the relative impacts of vascular and nerve injury that culminate in erectile dysfunction in a pilot study using a rat model of prostate irradiation and a thrombopoietin mimetic. *Int. J. Radiat. Oncol. Biol. Phys.* **103**, 1212–1220 (2019).
55. H. Kang, Sample size determination and power analysis using the G*Power software. *J. Educ. Eval. Health.* **18**, 17 (2021).
56. G. An *et al.*, Functional reconstruction of injured corpus cavernosa using 3D-printed hydrogel scaffolds seeded with HIF-1α-expressing stem cells. *Nat. Commun.* **11**, 2687 (2020).
57. S. Wang, Data from "Single-cell RNA sequencing of rat corpus cavernosum." Sequence Read Archive. https://www.ncbi.nlm.nih.gov/sra/PRJNA1172004. Deposited 12 October 2024.